

Gyrotactic bioconvection in three dimensions

S. Ghorai

Department of Mathematics and Statistics, Indian Institute of Technology, Kanpur 208016, India

N. A. Hill

Department of Mathematics, University of Glasgow, Glasgow G12 8QW, United Kingdom

(Received 6 September 2006; accepted 23 March 2007; published online 17 May 2007)

The bioconvection equations, based on the continuum model of Pedley *et al.* [J. Fluid Mech. **195**, 223 (1988)], consist of the Navier-Stokes equations for an incompressible fluid coupled with a micro-organism conservation equation. These equations are solved efficiently using a semi-implicit second-order accurate conservative finite-difference method. The structure and stability of a three-dimensional plume in deep rectangular boxes with stress-free sidewalls are investigated. Comparisons are made with the two-dimensional and axisymmetric bioconvection. In deep chambers, the three-dimensional plume that forms initially along the central axis of the chamber typically breaks down via a meandering instability. © 2007 American Institute of Physics.
[DOI: 10.1063/1.2731793]

I. INTRODUCTION

Bioconvection is the name given to spontaneous pattern formation in suspensions of swimming micro-organisms such as bacteria and algae.^{1,2} In all cases, the micro-organisms are slightly denser than water and on average they swim upwards (although the reasons for up-swimming may be different for different species). Micro-organisms respond to certain stimuli by tending to swim in particular directions. These responses are called *taxes*, examples being *gravitaxis*, *gyrotaxis*, *phototaxis*, and *chemotaxis*. Gravitaxis, chemotaxis, and phototaxis, respectively, indicate swimming in the opposite sense to gravity, up a chemical gradient and toward or away from light. Gyrotaxis is swimming directed by the balance between the torque due to gravity acting on a bottom-heavy cell and the torque due to viscous forces arising from local shear flows. The bioconvection pattern reflects the presence of sinking and rising fluid columns similar to convection columns caused by a temperature gradient in a fluid. In bioconvection, they form because a horizontal layer of more dense cell-saturated fluid above a less dense fluid layer is an unstable configuration. This paper deals with gyrotactic bioconvection.

Experiments have discovered many fascinating and poorly understood examples of pattern formation in bioconvection.³⁻⁷ Large numbers of the bacterium *Bacillus subtilis* in a layer of water organize into quasiperiodic patterns. The first instability to occur in a culture of the alga *Chlamydomonas nivalis* usually consists of sheets or lines when viewed from above. The sheet instability usually breaks down to a dot-type instability or a pattern resembling a lattice of nodes joined by lines.⁸ These patterns again break down to smaller dots or other connected patterns. Wager³ reported that a suspension of the alga *Euglena gracilis* illuminated from above and the side accumulated on the surface forming a series of ripple-like aggregations moving toward the light, which persisted until all the cells had reached the side of the vessel. The patterns' shapes and sizes depend on

many parameters such as cell concentration, depth of the fluid layer, and swimming speed. Because many of the observed phenomena such as quasiperiodic patterns are difficult to analyze mathematically, there is a need to develop numerical algorithms that can simulate these experiments.

Most of the bioconvection experiments were performed in large aspect ratio chambers (ratio of horizontal width to depth). Simulation in a large aspect ratio chamber offers a significant computational challenge. The number of mesh points must be large to resolve the spatial features of the flow and the simulations need to be run over a long period of time to eliminate the transient behavior of the solutions. Most often the swimming velocity of the micro-organisms is a function of the fluid velocity field, which must be calculated at each time step. In advanced bioconvection models, the diffusivity of the micro-organisms is also a function of the fluid velocity field. Thus efficient algorithms are essential for studying bioconvection in a large aspect ratio chamber.

Because of these computational difficulties, there have been no bioconvection simulations in three dimensions to date. All of the previous simulations were carried out in two dimensions. Harashima *et al.*⁹ simulated gravitactic bioconvection in two dimensions and studied the evolution of bioconvection from an initially uniform state. Their computational domain had a width/height aspect ratio of 8. Ghorai and Hill¹⁰⁻¹² carried out computations of gyrotactic bioconvection in two dimensions. They also studied gyrotactic bioconvection in an axisymmetric chamber.¹³ All the computations mentioned above were based on continuum models. Recently, Hopkins and Fauci¹⁴ simulated two-dimensional bioconvection using point particles.

Although it is relatively easy to solve the two-dimensional problem, bioconvection is intrinsically three-dimensional. The bioconvection pattern, for example, has polygonal cells (e.g., squares, hexagons) each with a narrow descending central core surrounded by a broad column of rising fluid. Note that axisymmetric bioconvection¹³ provides the simplest three-dimensional configuration, but the axisym-

metric model has limitations. First, the bioconvection cells rarely have a circular boundary assumed in the axisymmetric model. Second, the axisymmetric configuration suppresses the meandering mode of the plumes that has been observed in deep chambers. We have therefore investigated a realistic three-dimensional bioconvection model confined between stress-free sidewalls. A chamber with large horizontal cross-sectional area will generate several plumes. The aim of the present computation is to study the structure and stability of just one of them.

II. MATHEMATICAL FORMULATION

Consider the motion of a suspension of micro-organisms in a rectangular chamber with the z axis pointing upwards. As in Pedley *et al.*,¹⁵ we assume a monodisperse cell population modeled by a continuous distribution. The suspension is dilute, so that the volume fraction of the cells is small and cell-cell interactions are negligible. Each cell has a volume ϑ and density $\rho + \delta\rho$, where ρ is the density of the water in which the cells swim and $\delta\rho/\rho \ll 1$.

A. Governing equations

Let \mathbf{u} , n , and W_c denote, respectively, the fluid velocity, cell concentration, and constant cell swimming speed. The suspension is incompressible, hence

$$\nabla \cdot \mathbf{u} = 0. \quad (1)$$

The momentum equations under the Boussinesq approximation become

$$\rho \left(\frac{\partial \mathbf{u}}{\partial t} + (\mathbf{u} \cdot \nabla) \mathbf{u} \right) = -\nabla p_e - \delta\rho \vartheta n g \hat{\mathbf{z}} + \nabla \cdot \boldsymbol{\Sigma}, \quad (2)$$

where p_e is the excess pressure above hydrostatic, g is the value of the acceleration due to gravity, $\boldsymbol{\Sigma}$ is the bulk deviatoric stress tensor, and $\hat{\mathbf{z}}$ is a unit vector directed vertically upwards. The swimming of the cells contributes extra stresses to the bulk deviatoric stress tensor.¹⁶ In a dilute suspension, the only significant contribution to $\boldsymbol{\Sigma}$, other than the Newtonian stress, is that derived from the stresslets associated with the cells' intrinsic motions.¹⁶ This extra stress term, associated with the cells' locomotion, is much smaller than the Newtonian stress. Also it should be calculated from generalized Taylor dispersion theory,^{17,18} but no complete theory exists for all flows. Thus the stress associated with cells' locomotion is neglected and this simplification is needed to make realistic computational progress. Thus as in Pedley *et al.*,¹⁵ we assume

$$\boldsymbol{\Sigma} = 2\mu \mathbf{E}, \quad (3)$$

where \mathbf{E} is the bulk rate of strain tensor and μ is the fluid viscosity.

Conservation of cells requires that

$$\frac{\partial n}{\partial t} = -\nabla \cdot \mathbf{J}, \quad (4)$$

where the flux of cells is

$$\mathbf{J} = n\mathbf{u} + nW_c \bar{\mathbf{p}} - D \nabla n. \quad (5)$$

The third term on the right-hand side of Eq. (5) represents the random component of the cell locomotion. Here the diffusion coefficient D is assumed to be constant. $W_c \bar{\mathbf{p}}$ is the average swimming velocity relative to the fluid, and $\bar{\mathbf{p}}$ represents the average orientation of cells.

The equations are scaled using L (a dimension of the box), L^2/D , D/L , $\rho D^2/L^2$, and \bar{n} (mean concentration) as the scale factors for length, time, velocity, pressure, and concentration, respectively. The resulting system of coupled equations becomes

$$\nabla \cdot \mathbf{u} = 0, \quad (6)$$

$$\frac{\partial \mathbf{u}}{\partial t} = -(\mathbf{u} \cdot \nabla) \mathbf{u} - \nabla p_e + S_c \nabla^2 \mathbf{u} - S_c R n \hat{\mathbf{z}}, \quad (7)$$

$$\frac{\partial n}{\partial t} = -\nabla \cdot (n\mathbf{u} + nV_c \bar{\mathbf{p}}) + \nabla^2 n, \quad (8)$$

where $S_c = \nu/D$ is the Schmidt number, $R = \bar{n} \vartheta \Delta \rho g L^3 / \rho \nu D$ is the Rayleigh number, and $V_c = W_c L/D$ is the scaled swimming speed. This scaling is chosen for consistency and comparison with previously published work.^{10-12,19,20} The equations can also be scaled using the cell swimming speed W_c instead of D , but values of both quantities need to be measured when comparing numerical results with experiments.

B. Average orientation

For simplicity, algal cells such as *Chlamydomonas* (whose shape closely approximates a spheroid) are idealized here as spheres of radius a . Figure 1 shows such a cell placed in a fluid flow. Let the unit vector \mathbf{p} point in the swimming direction of the cell. The cells are bottom-heavy so that the center of mass is displaced from the center of buoyancy. The force of gravity, acting through the center of mass, exerts a torque $\mathbf{T}_g = -h m \mathbf{p} \times \mathbf{g}$, where m and \mathbf{g} are the mass of the cell and acceleration due to gravity, respectively. The viscous

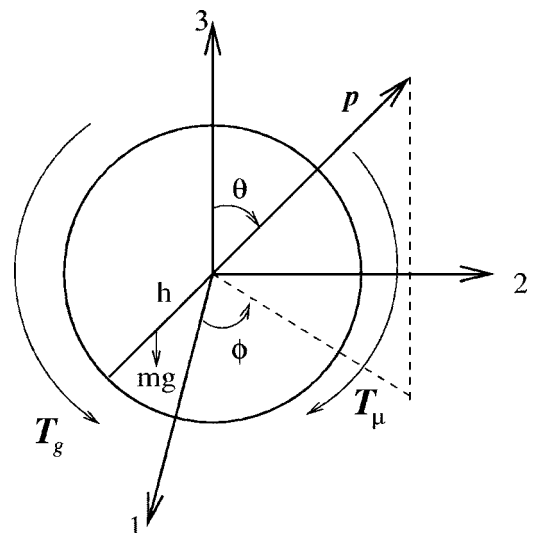


FIG. 1. An idealized algal cell. Representation of the orientation vector \mathbf{p} by means of spherical-polar angles θ and ϕ relative to a right-handed system of Cartesian coordinates with origin at the center. Here h denotes the distance of the center of gravity from the center of the cell.

torque on a sphere of radius a in a fluid of viscosity μ is given by

$$\mathbf{T}_\mu = 4\pi\mu a^3(\nabla \times \mathbf{u} - 2\mathbf{\Omega}), \quad (9)$$

where $\mathbf{\Omega}$ is the sphere's angular velocity. If the cells are idealized as spheroids instead of spheres, then an extra term involving rate of strain should be added to the right-hand side of Eq. (9).¹⁶

Since the inertial effects are negligible at the low Reynolds number flow associated with the motion of the cells, their orientation is specified by $\mathbf{T}_g + \mathbf{T}_\mu = 0$. This leads to the equation for the reorientation rate,²¹

$$\dot{\mathbf{p}} = \frac{1}{2B}[\hat{\mathbf{z}} - (\hat{\mathbf{z}} \cdot \mathbf{p})\mathbf{p}] + \frac{\boldsymbol{\omega} \times \mathbf{p}}{2}, \quad (10)$$

where $\boldsymbol{\omega}$ is the local vorticity field and $B = 4\pi\mu a^3/mgh$ is called the gyrotactic reorientation parameter. The equations describing the equilibrium orientation are

$$-\omega_1 \sin \phi + \omega_2 \cos \phi = \sin \theta/B, \quad (11)$$

$$\omega_1 \cos \phi + \omega_2 \sin \phi = \omega_3 \tan \theta$$

(Ref. 22). Let $\omega = |\boldsymbol{\omega}|$ denote the magnitude of the vorticity vector. For flows with $\omega_3 = 0$, there exists a stable equilibrium with $\sin \theta = B\omega$ if $B\omega < 1$, but no stable equilibrium if $B\omega > 1$. When $B\omega > 1$, the cells tumble and the average swimming direction $\bar{\mathbf{p}}$ is obtained by integrating \mathbf{p} over a tumbling period.¹⁰ However, for $\omega_3 \neq 0$, the equilibrium is always stable. The average swimming direction $\bar{\mathbf{p}}$ is equal to \mathbf{p} when the equilibrium is stable. After scaling, the dimensionless gyrotaxis number is given by

$$G = \frac{BD}{L^2},$$

which represents the ratio of the reorientation time due to gyrotaxis to the diffusion time. A practical demonstration of the gyrotactic mechanism is that the cells swim toward the axis and focus into a narrow beam for Poiseuille flow down a cylinder. Conversely, if the direction of the flow is reversed, the cells accumulate along the periphery of the cylinder, confirming the role of gyrotaxis in the orientation.²³

C. Initial and boundary conditions

We now turn to the boundary conditions for these equations, which are to be integrated in the three-dimensional region bounded by the planes $x=0, \lambda_x$, $y=0, \lambda_y$, and $z=0, \lambda_z$. Here λ_x , λ_y , and λ_z are the aspect ratios in the Cartesian x , y , and z directions, respectively. A rigid no-slip boundary condition is imposed at the bottom wall and the other boundaries are stress-free. If $\mathbf{u} = (u, v, w)$, then these boundary conditions can be written as

$$\frac{\partial w}{\partial x} = \frac{\partial v}{\partial x} = u = 0 \quad \text{at } x = 0, \lambda_x,$$

$$\frac{\partial u}{\partial y} = \frac{\partial w}{\partial y} = v = 0 \quad \text{at } y = 0, \lambda_y,$$

$$u = v = w = 0 \quad \text{at } z = 0, \quad \frac{\partial u}{\partial z} = \frac{\partial v}{\partial z} = w = 0 \quad \text{at } z = \lambda_z.$$

The boundary condition on n is that there be no flux of cells through the walls, thus

$$\mathbf{J} \cdot \hat{\mathbf{n}} = 0 \quad \text{at } x = 0, \lambda_x; y = 0, \lambda_y; z = 0, \lambda_z;$$

where \mathbf{J} is the flux of the cells and $\hat{\mathbf{n}}$ is the unit normal to the respective plane.

The initial conditions are that of a uniform state together with a small perturbation to the uniform concentration of cells,

$$\mathbf{u} = 0, \quad \text{and } n = 1 + \epsilon \sin\left(\frac{\pi x}{\lambda_x}\right) \sin\left(\frac{\pi y}{\lambda_y}\right),$$

where $\epsilon = 10^{-10}$. The perturbation is applied so that the plume forms along the center of the chamber.

III. NUMERICAL PROCEDURE

We use a semi-implicit conservative finite-difference implementation of a second-order projection method.²⁴ The governing equations are discretized on a staggered grid. We take a uniform mesh in the horizontal directions. There are boundary layers at the top and bottom walls due to large cell concentration and the presence of the rigid wall, respectively. In order to resolve these gradients accurately, a nonuniform mesh is used in the vertical direction. All the spatial derivatives are computed using central difference relations for non-uniform grids. Suppose that the solutions n^k and \mathbf{u}^k at the k th time step $t_k = k\Delta t$ with $k \geq 0$ are known. The time integration from t_k to $t_{k+1} = t_k + \Delta t$ consists of the following steps:

- (i) Calculate the concentration field by

$$\frac{n^{k+1} - n^k}{\Delta t} + \frac{1}{2}[3H_n^k - H_n^{k-1}] = \frac{\nabla^2 n^{k+1} + \nabla^2 n^k}{2}, \quad (12)$$

where the nonlinear advective term $H_n = \nabla \cdot (\mathbf{u}n + V_c \bar{\mathbf{p}}n)$ is discretized using a second-order Adams-Bashforth scheme and an implicit Crank-Nicholson step is applied to the diffusion term.

- (ii) Calculate the intermediate velocity field \mathbf{u}^* with pressure $p_e^{k-1/2}$:

$$\frac{\mathbf{u}^* - \mathbf{u}^k}{\Delta t} + \frac{1}{2}[3H_u^k - H_u^{k-1}] = -\nabla p_e^{k-1/2} + S_c \frac{\nabla^2 \mathbf{u}^* + \nabla^2 \mathbf{u}^k}{2} - S_c Rn^{k+1/2} \hat{\mathbf{z}}, \quad (13)$$

where the nonlinear advective, the viscous diffusion, and the buoyancy terms are advanced using Adams-Bashforth, Crank-Nicholson, and Adams-Moulton schemes, respectively.

- (iii) Perform the projection

$$\frac{\mathbf{u}^{k+1} - \mathbf{u}^*}{\Delta t} = -\nabla \chi, \quad \nabla \cdot \mathbf{u}^{k+1} = 0. \quad (14)$$

The use of the incompressibility condition $\nabla \cdot \mathbf{u}^{k+1} = 0$ leads to the Poisson problem for χ ,

$$\nabla^2 \chi = \frac{\nabla \cdot \mathbf{u}^*}{\Delta t}, \quad (15)$$

subject to $\partial\chi/\partial n=0$ on the walls. Solve the Poisson equation for χ and update the velocity field using the first relation in Eq. (14).

- (iv) Update the pressure using the modified pressure increment equation,²⁵

$$p_e^{k+1/2} = p_e^{k-1/2} + \chi - S_c \frac{\Delta t}{2} \nabla^2 \chi. \quad (16)$$

The transport equations (12) and (13) are solved using an approximate factorization method. The solution of the Poisson equation (15), which is the most time-consuming part of the algorithm, is obtained in two steps. The application of the fast Fourier transform (FFT)²⁶ in the horizontal directions reduces the problem to a system of uncoupled tridiagonal matrix equations in the vertical direction. These equations are inverted in the usual manner and then the solution is reconstructed via inverse Fourier transform. The mesh size is 32×32 in the horizontal and the number of grid points along the z direction is increased with an increase in the vertical aspect ratio λ_z . For example 32, 64, and 128 points are taken for $\lambda_z=1, 2,$ and $4,$ respectively. Some of the results were run with a 64×64 grid in the horizontal plane and more grid points in the vertical direction to check the grid independence of the solutions. Due to the FFT, we always use 2^p (p being a positive integer) grid points in the horizontal directions. The code can be applied with minor changes to the two-dimensional problem and can be modified to study other flow problems. The two-dimensional results for the flow in a driven cavity agree well with those given in Refs. 27 and 28. Also, the agreement of the results of natural convection in three dimensions with those of Fusesgi *et al.*²⁹ is good.

IV. RESULTS

Equations (6)–(8) possess a static equilibrium solution with $\mathbf{u}=\mathbf{0}$ and an exponential concentration profile

$$n_s(z) = \frac{V_c \lambda_z \exp(V_c z)}{\exp(V_c \lambda_z) - 1}. \quad (17)$$

The system is governed by the parameters $R, V_c, G, S_c, \lambda_x, \lambda_y,$ and λ_z . An infinitesimal disturbance to the static solution either dies down (a linearly stable state) or grows in

TABLE I. Estimates of typical parameters for a suspension of alga *Chlamydomonas nivalis*.

Cell radius	a	10^{-3} cm
Cell volume	ϑ	5×10^{-10} cm ³
Cell density ratio	$\delta\rho/\rho$	5×10^{-2}
Cell diffusivity	D	5×10^{-4} cm ² s ⁻¹
Gyrotactic parameter	B	3.4 s
Swimming speed	W_c	10^{-2} cm s ⁻¹
Mean concentration	\bar{n}	10^6 cm ⁻³
Kinematic viscosity	ν	10^{-2} cm ² s ⁻¹

amplitude (a linearly unstable state) depending on the parameter values. The critical parameter values separate the two classes of states. If the governing parameters are above critical values, the concentration profile develops from initially uniform state toward Eq. (17), but bioconvection begins before the profile develops fully. The following discussions are based on a three-dimensional chamber whose horizontal cross section is square. We consider physically relevant parameter values using data from Table I based on estimates given by Kessler.³⁰

A. Effect of the depth

The parameter values

$$S_c = 20, \quad V_c = 10, \quad G = 0.01, \quad R = 500, \quad \lambda_x = \lambda_y = 1 \quad (18)$$

are kept constant and the depth parameter λ_z is varied from small to large values. The same parameter values were used in previous two-dimensional and axisymmetric bioconvection simulations (Refs. 10 and 13).

Figure 2 shows an example of the initial evolution of cell concentration in the z direction and also the solution given by Eq. (17). At $t=0$, the concentration is uniform and $n=1$ approximately. The concentration at the top (bottom) of the chamber increases (decreases) with time due to cells swimming upwards toward the top of the chamber where a zero cell-flux condition holds. As time increases, the concentration profile tends to the exponential profile [see Eq. (17)]. Since the parameters are above the critical values, a plume begins to form (and the solutions become functions of x, y also) before the equilibrium exponential profile is achieved.

Figure 3 shows the evolution of the plume at various times after the initial uniform state. In these diagrams, we have plotted the concentration as isosurfaces. The plume starts to form around $t=0.32$ [Fig. 3(a)] and begins descend-

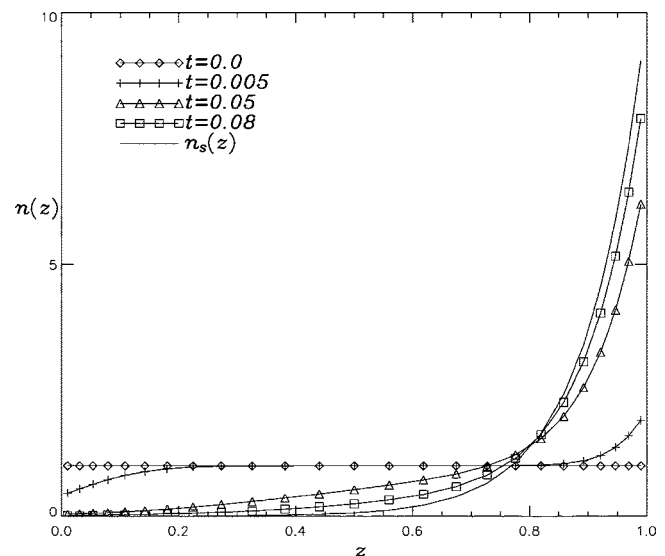


FIG. 2. Evolution of the cell concentration $n(z)$, in the midvertical line, for an ultimately unstable suspension at an early stage for $\lambda_z=1, G=0.01, V_c=10,$ and $R=500$. Here $n_s(z)$ is the equilibrium concentration profile [see Eq. (17)].

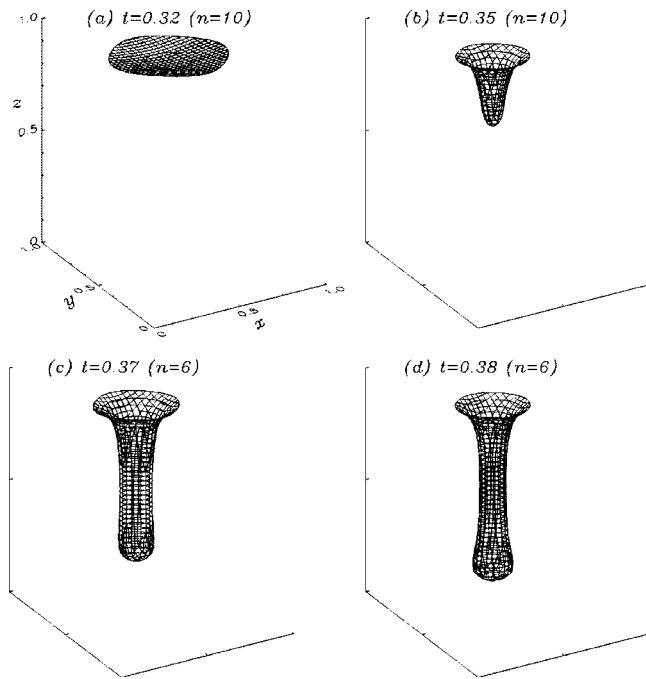


FIG. 3. Gyrotactic plume formation for the suspension shown in Fig. 2 for $\lambda_z=1$, $G=0.01$, $V_c=10$, and $R=500$. The concentration $n(x,y,z)$ at different times is plotted as isosurfaces. Value inside the parentheses indicates the value of the isosurface.

ing [Fig. 3(b)]. It hits the bottom of the chamber at $t \approx 0.38$ and becomes steady rapidly. The final steady state of the plume and the vertical velocity at the midheight plane are shown in Fig. 4. The concentration in the steady state is less steep across the plume compared to the initial stage. The plume is qualitatively similar to the axisymmetric plume.¹³

For $\lambda_z=2$, the initial evolution of the plume is similar to the $\lambda_z=1$ case. The variation of the central concentration

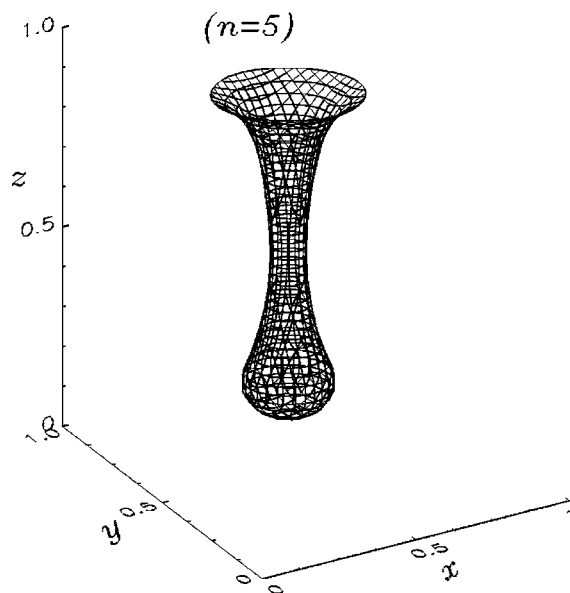


FIG. 4. Steady-state concentration $n(x,y,z)$ and vertical velocity $w(x,y,1/2)$ for $\lambda_z=1$, $G=0.01$, $V_c=10$, and $R=500$. The concentration is plotted as an isosurface and the vertical velocity as contours.

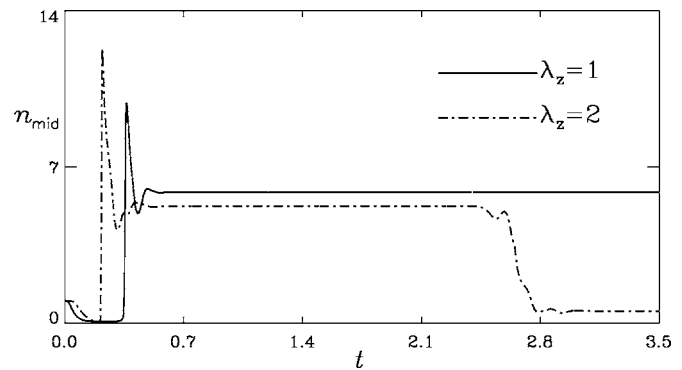
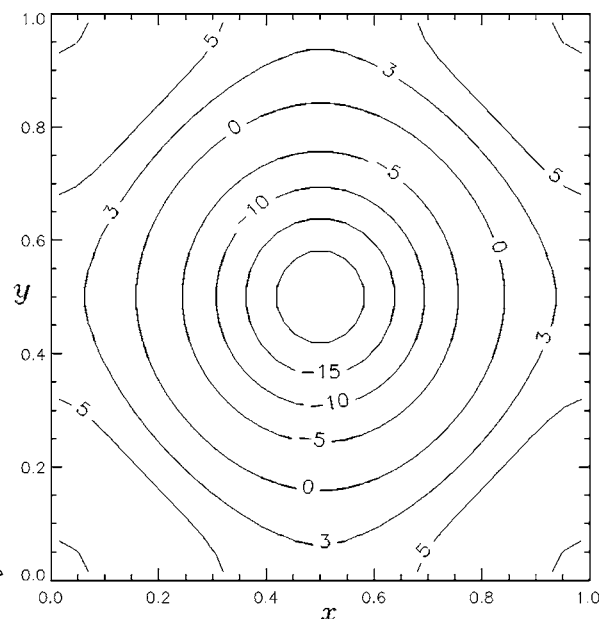


FIG. 5. Variation of central concentration at the midheight of the chamber for two different values of the aspect ratio λ_z . The drop in concentration around $t=2.7$ for $\lambda_z=2$ indicates that the plume has shifted from the central position of the chamber via a meandering instability. The other parameter values are $G=0.01$, $V_c=10$, and $R=500$.

against time is compared with that of $\lambda_z=1$ (Fig. 5). The large values of the central concentration at around $t=0.36$ and 0.22 are the concentrations at the heads of the plumes for $\lambda_z=1$ and 2 , respectively, when they pass through the central point. The solution for $\lambda_z=2$ then remains for some time apparently in a steady state similar to the $\lambda_z=1$ case, but ultimately a “meandering” instability develops. The snapshots of the plume for $\lambda_z=2$ at $t=1.6$ (apparent steady state) and $t=2.65$ (meandering instability) are shown in Fig. 6. When the plume is in the apparently steady state, then the solution in the interior is almost independent of the vertical coordinate z [Fig. 6(a)]. The horizontal fluid flow field and cell flux in the apparently steady state and meandering state are shown in Figs. 7 and 8. In the apparently steady state, both the horizontal fluid velocity and cell flux converge into the central axis of the plume (Fig. 7). In the meandering



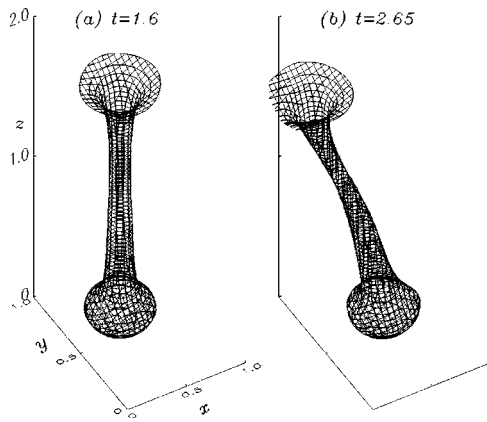


FIG. 6. Snapshots of (a) apparent steady state and (b) growth of meandering instability for vertical aspect ratio $\lambda_z=2$, $G=0.01$, $V_c=10$, and $R=500$. The concentration is plotted as an isosurface ($n=4.2$).

state, the cell flux converges into the plume but the horizontal flow moves away from the plume. Further, the cell flux converges to a noncentral point inside the plume. The plume breaks into two plumes, which move to the opposite corners of the chamber, which is a final steady state (Fig. 9).

The numerical calculations are performed with different mesh sizes and time steps for $\lambda_z=2$. It is observed that sometimes the plume moves to one corner of the chamber only, which is also a final steady state. Also the initial, symmetry breaking, meandering movement of the plume is arbitrary and is not necessarily toward a corner of the chamber. The time required for a plume to shift to corner(s) of the chamber depends on the direction of the meanders of the plume. Thus a plume, whose direction of initial meander is perpendicular to a wall, takes more time to move to corner(s) of the chamber than that whose direction of initial meander is toward the corner. The variation of the central concentration is compared for two different mesh sizes for $\lambda_z=2$ in Fig. 10. The solid line represents the value on a $64 \times 64 \times 128$ mesh without refinement in the vertical direction. The dotted line and

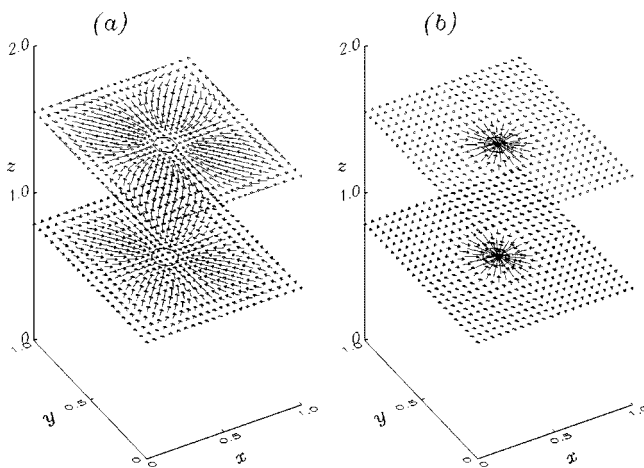


FIG. 7. (a) Horizontal fluid flow field and (b) horizontal cell flux in the apparently steady state [Fig. 6(a)]. The closed contours indicate the plume location and correspond to the concentration $n=4.2$. Arrows indicate the direction of the horizontal flow or horizontal cell flux and the magnitude is proportional to their lengths.

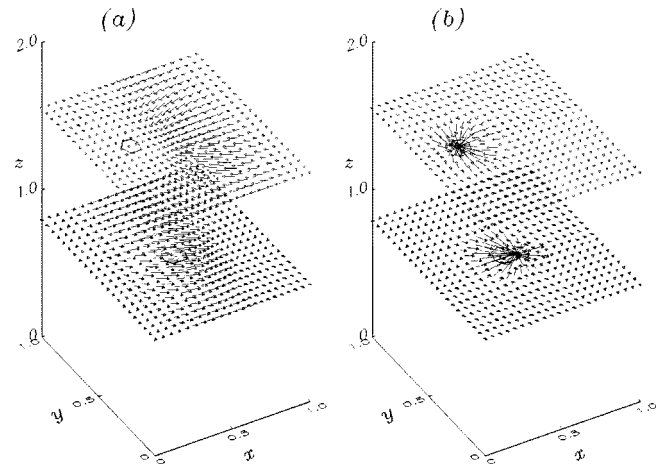


FIG. 8. (a) Horizontal fluid flow field and (b) horizontal cell flux in the meandering state [Fig. 6(b)]. The closed contours indicate the plume location and correspond to the concentration $n=4.2$. Arrows indicate the direction of the horizontal flow or horizontal cell flux and the magnitude is proportional to their lengths.

the dash-dotted line correspond to the value on a $32 \times 32 \times 64$ mesh with refinement in the vertical direction. The time step Δt equals 2×10^{-5} for the solid and dash-dotted line and equals 4×10^{-5} for the dotted line. The final steady state is that of two plumes in the opposite corner of the chamber for the solid and dotted lines. The dash-dotted line corresponds to a steady single plume in a corner of the chamber. The differences in the time, for the plume to shift to corner(s) of the chamber, are due to the direction of the initial meander of the plume. To illustrate the accuracy of the mesh, the properties of the steady solution with two plumes in the opposite corners are compared in Table II. The quantities given in Table II are the following:

- (i) The value of the central concentration.
- (ii) The maximum value of vertical velocity w on the line $x=y=1/2$, together with its location.
- (iii) The maximum value of the vorticity component ω_1 on the rigid boundary ($z=0$), together with its location.

The positions of the maximum are obtained using polynomial interpolation. It is seen from Table II that two-figure accuracy is achieved with the $32 \times 32 \times 64$ grid.

When the vertical aspect ratio is increased to $\lambda_z=4$, the three-dimensional plume again undergoes a meandering instability from an apparently steady state, similar to the $\lambda_z=2$ case. But in this case, the final state of the solution is sometimes unsteady, unlike the final states observed for $\lambda_z=2$.

For the parameter values given in Eq. (18), the characteristics of the solutions versus the two-dimensional and axisymmetric results (Refs. 10 and 13) are the following:

- (i) The solutions approach a steady-like state rapidly, which is similar to the axisymmetric solutions. But the two-dimensional solution is different. For vertical aspect ratio 1, the solution becomes steady rapidly.

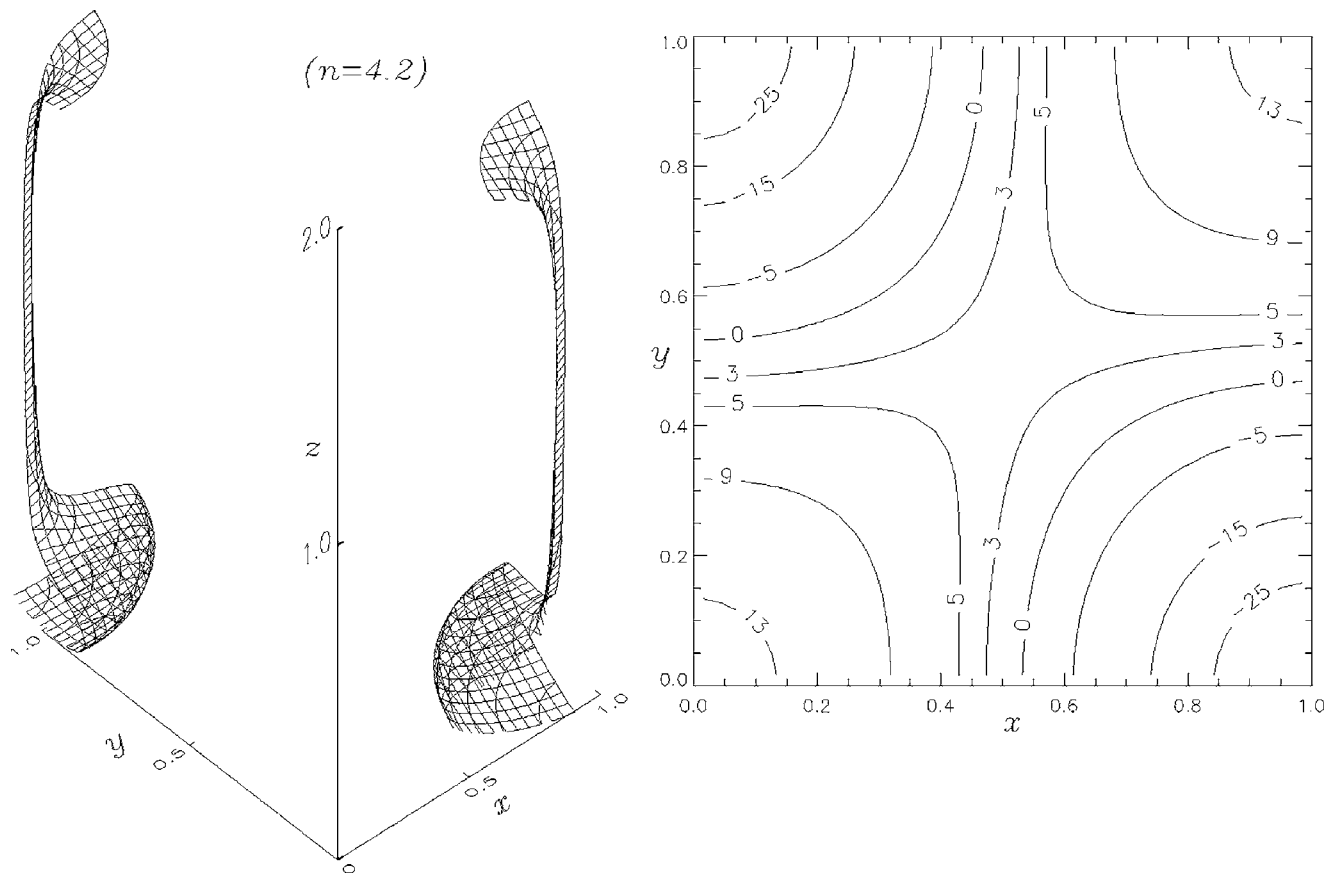


FIG. 9. Steady-state concentration $n(x,y,z)$ and vertical velocity $w(x,y,1)$ for $\lambda_z=2$, $G=0.01$, $V_c=10$, and $R=500$. The concentration is plotted as an isosurface and the vertical velocity as contours.

For vertical aspect ratios in the range from 2 to 3, a small “blob” or varicose instability develops that ultimately disappears slowly with an increase in the value of vertical aspect ratio leading to an apparent steady state. Periodic “blob” convection is observed for vertical aspect ratio greater than or equal to 4.

- (ii) Ultimately the meandering instability breaks down the plume in a similar way to the two-dimensional results. The axisymmetric solution is independent of the azi-

muthal coordinate. Due to this imposed symmetry, the meandering instability does not occur in the axisymmetric case.

- (iii) The plume moves to one of the side walls via meandering instability in the two-dimensional case. But here the plume either moves to a single corner or breaks into two plumes that move to opposite corners of the chamber.

However, there are ranges of parameter values where periodic “blob” convection is observed in the initial stages in these three-dimensional calculations. For example, we consider the following parameter values:

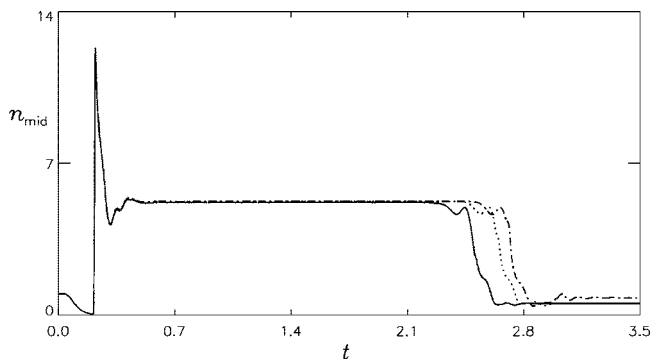


FIG. 10. Comparison of the variation of central concentration for different mesh sizes and time steps (see text for details) for $\lambda_z=2$, $G=0.01$, $V_c=10$, and $R=500$. The drop in concentration indicates that the plume has shifted from the central position of the chamber via a meandering instability. The differences in the time, for the plume to shift to corner(s) of the chamber, are due to the direction of the initial meander of the plume.

TABLE II. Properties of the solution of the final steady state with plumes in the opposite corners of the chamber using different grids. The parameter values are $\lambda_z=2$, $R=500$, $V_c=10$, and $G=0.01$.

Grid	Nodes	n_{mid}	$w_{max}(x=y=1/2)$ (z)	$\omega_{1,max}(z=0)$ (x,y)
Stretched	$32 \times 32 \times 64$	0.546	6.429 (0.397)	192.5 (0, 0.705)
Uniform	$64 \times 64 \times 128$	0.546	6.406 (0.397)	192.4 (0, 0.704)

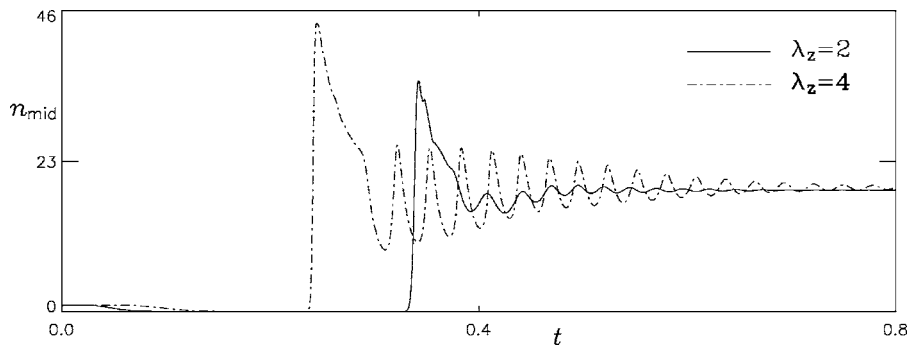


FIG. 11. Variation of central concentration at the initial stages for different values of the vertical aspect ratio. The other parameter values are $G=0.008$, $V_c=20$, and $R=250$.

$$S_c = 20, \quad V_c = 20, \quad G = 0.008, \quad R = 250, \quad \lambda_x = \lambda_y = 1. \quad (19)$$

The variation of the central concentration at the initial stages, for vertical aspect ratios $\lambda_z=2$ and 4, is shown in Fig. 11. The fluctuations in the concentrations in Fig. 11 are due to the passing of the blobs through the central point of the chamber. Figure 12 shows the snapshot of periodic blob convection at $t=0.36$ for vertical aspect ratio $\lambda_z=4$. The blobs disappear and lead to the apparently steady state, though the fluctuations take longer to disappear for $\lambda_z=4$. Ultimately, the meandering instability sets in all cases and the plumes move away from the center of the chamber. In two-dimensional simulations with a large aspect ratio chamber, the meandering instability sets in while the blob convection is in progress. In contrast, in three dimensions, the meandering instability sets in during the apparent steady state, after the early blob convection disappears.

B. Parametric dependence

Due to the large number of parameters, it is expensive to obtain a comprehensive picture across the whole parameter domain, so here we choose to investigate the dependence of

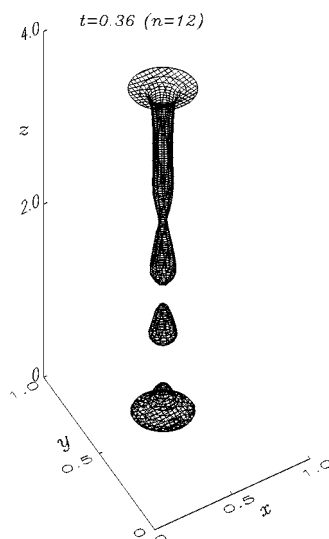


FIG. 12. Snapshot of periodic blob convection: isosurfaces for vertical aspect ratio $\lambda_z=4$. The other parameter values are $G=0.008$, $V_c=20$, and $R=250$.

the solutions on G and V_c for a chamber of fixed size $\lambda_x = \lambda_y = 1$ and $\lambda_z=5$. The parameter values using data in Table I based on a length scale (L) of 0.5 cm are

$$S_c = 20, \quad R = 250, \quad G = 0.007, \quad V_c = 10.$$

We now vary G from 0.002 to 0.011 and V_c from 5 to 20 to cover a range of physically relevant parameter values. We choose $V_c=5, 10, 15, 20$ and $G=0.002, 0.005, 0.008, 0.011$, respectively, as the representative values of V_c and G . In all cases, the central plume is subject to the meandering instability. Here we describe the details of the characteristics of the solutions at the initial stage for $V_c=15$. All the calculations are carried out in a $64 \times 64 \times 136$ mesh.

The variation of the concentration at a point on the central vertical line for $V_c=15$ is shown in Fig. 13. Since the length of the plume does not extend to the middle of the chamber for $G=0.002$, the corresponding point on the axis is taken at height 4. Figure 13 shows that for a fixed value of V_c , the time to reach the overturning instability stage decreases with an increase in the value of G . The fluctuations in the concentrations correspond to the varicose instability (“blobs”), which disappears, leading to the apparent steady state and then the meandering instability sets in. The snapshots of the plumes at $t=0.8$ for different values of G are shown in Fig. 14. The combined effects of cell swimming and gyrotaxis are weaker for smaller values of G , and in such cases the plumes extend only to a fraction of the chamber’s depth. The amplitude of the fluctuations is large for intermediate values of G and diminishes again at the highest value of G . For large G , the fluctuations are small since most of the cells, after reaching the bottom of the chamber, are forced to remain there due to the strong circulation at the bottom boundary. The results for other values of G and V_c in the initial stage can be summarized as follows. The plumes do not extend to the middle of the chamber for $V_c=5$ and $0.002 \leq G \leq 0.011$. Similar results are observed for $G=0.002$ and $5 \leq V_c \leq 20$. The varicose instability (blob convection) is observed when $G=0.005$, $V_c=20$; $G=0.008$, $V_c=15, 20$; and $G=0.11$, $V_c=15$. Thus the varicose instability is usually associated with intermediate values of G and higher values of V_c . Similar characteristics are observed in the two-dimensional and axisymmetric cases as well.

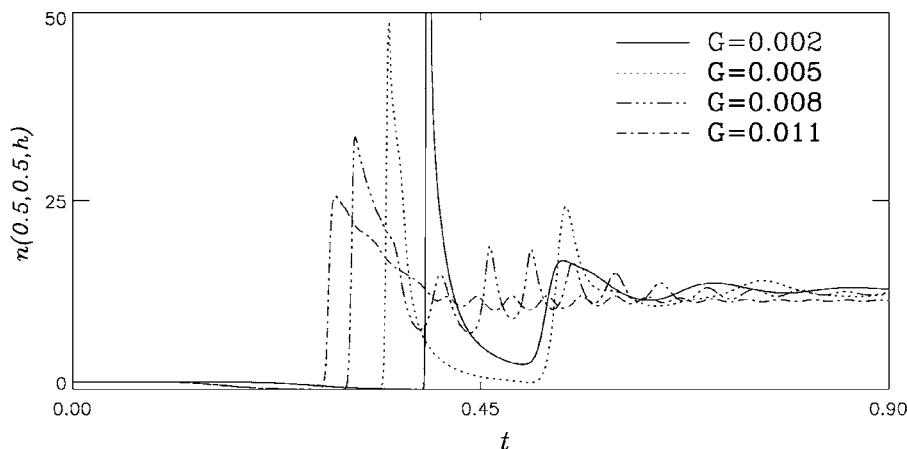


FIG. 13. Variation of the concentration at height h on the central vertical axis of the chamber for different values of G during the initial stages. The height $h=2.5$, except for $G=0.002$ when $h=4$. The other parameter values are $\lambda_z=5$, $V_c=15$, and $R=250$.

V. CONCLUSIONS

In this work, we have presented a semi-implicit second-order accurate conservative finite-difference method to integrate the bioconvection equations in three dimensions. In deep chambers, the plume becomes unstable either via varicose or meandering instability. The varicose instability observed in three dimensions is similar to that of the axisymmetric solutions. The mechanism of varicose instability is the same as that of two-dimensional gyrotactic bioconvection (see Ref. 10). The time period of the varicose oscillation in axisymmetric bioconvection (and thus of three-dimensional bioconvection too) is more realistic than that of the two-dimensional bioconvection.¹³ On the other hand, the meandering instability (seen in two-dimensional bioconvection) does not appear in the axisymmetric case. The meandering mode has been observed in experiments with gyrotactic micro-organisms in deep chambers (see Fig. 4 in Ref. 31). Thus the three-dimensional results are closer to the experimental observations.

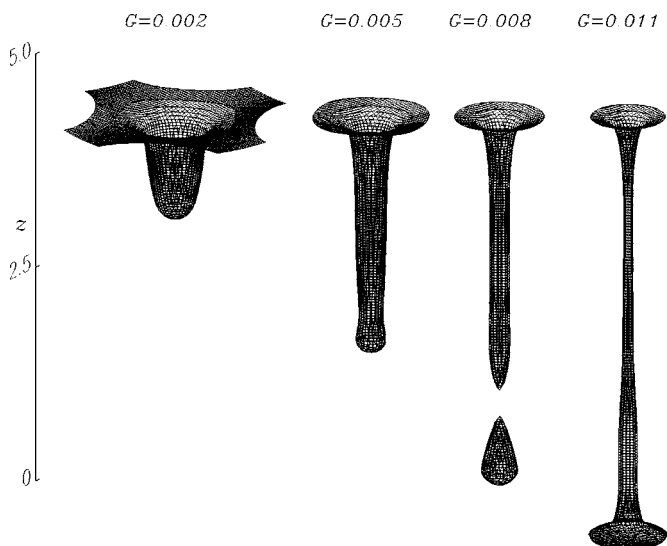


FIG. 14. Snapshots of concentrations (isosurface value $n=11$) at $t=0.8$ for different values of G . The other parameter values are $\lambda_z=5$, $V_c=15$, and $R=250$. Ultimately all the solutions become unstable via meandering instability.

The effects of depth on the stability of a single plume have been examined. We find a steady solution for a small vertical-aspect-ratio chamber. As the depth of the chamber is increased, we observed either apparently steady state or periodic blob convection in the initial stages depending on the parameter values. Ultimately the plumes are destabilized via a meandering instability. The characteristics of the solutions are similar to the axisymmetric results in the initial stages and two-dimensional results in the final stages.

The effects of G and V_c on the plume in deep chamber are examined for a range of physically relevant parameter values. When the values of either G or V_c are small, the plumes do not extend to the bottom of the chamber. A varicose instability is often observed in the initial stages for intermediate values of G and higher values of V_c . When G is high, the varicose instability almost disappears.

ACKNOWLEDGMENT

S.G. is grateful to the Department of Science and Technology (India) for a BOYSCAST fellowship held while part of this research was being carried out at the Department of Mathematics, University of Glasgow, UK.

¹T. J. Pedley and J. O. Kessler, "Hydrodynamic phenomena in suspensions of swimming microorganisms," *Annu. Rev. Fluid Mech.* **24**, 313 (1992).

²N. A. Hill and T. J. Pedley, "Bioconvection," *Fluid Dyn. Res.* **37**, 1 (2005).

³H. Wager, "The effect of gravity upon the movements and aggregation of *Euglena viridis*, Ehrb, and other microorganisms," *Philos. Trans. R. Soc. London, Ser. B* **201**, 333 (1911).

⁴J. B. Loeffler and R. B. Mefferd, "Concerning pattern formation by free-swimming microorganisms," *Am. Nat.* **86**, 325 (1952).

⁵J. J. Wille and C. F. Ehret, "Circadian rhythm of pattern formation in population of a free-swimming organism, *Tetrahymena*," *J. Protozool.* **15**, 789 (1968).

⁶M. Levandowsky, W. S. Childress, E. A. Spiegel, and S. H. Hunter, "A mathematical model of pattern formation by swimming microorganisms," *J. Protozool.* **22**, 296 (1975).

⁷J. O. Kessler, "Gyrotactic buoyant convection and spontaneous pattern formation in algal cell cultures," in *Nonequilibrium Cooperative Phenomena in Physics and Related Fields*, edited by M. G. Velarde (Plenum, New York, 1984), p. 241.

⁸M. A. Bees and N. A. Hill, "Wavelengths of bioconvection patterns," *J. Exp. Biol.* **200**, 1515 (1997).

⁹A. Harashima, M. Watanabe, and I. Fujishiro, "Evolution of bioconvection

- patterns in a culture of motile flagellates," *Phys. Fluids* **31**, 764 (1988).
- ¹⁰S. Ghorai and N. A. Hill, "Development and stability of gyrotactic plumes in bioconvection," *J. Fluid Mech.* **400**, 1 (1999).
- ¹¹S. Ghorai and N. A. Hill, "Periodic arrays of gyrotactic plumes in bioconvection," *Phys. Fluids* **12**, 5 (2000).
- ¹²S. Ghorai and N. A. Hill, "Wavelengths of gyrotactic plumes in bioconvection," *Bull. Math. Biol.* **62**, 429 (2000).
- ¹³S. Ghorai and N. A. Hill, "Axisymmetric bioconvection in a cylinder," *J. Theor. Biol.* **219**, 137 (2002).
- ¹⁴M. M. Hopkins and L. J. Fauci, "A computational model of the collective fluid dynamics of motile microorganisms," *J. Fluid Mech.* **455**, 149 (2002).
- ¹⁵T. J. Pedley, N. A. Hill, and J. O. Kessler, "The growth of bioconvection patterns in a uniform suspension of gyrotactic microorganisms," *J. Fluid Mech.* **195**, 223 (1988).
- ¹⁶T. J. Pedley and J. O. Kessler, "A new continuum model for suspensions of gyrotactic micro-organisms," *J. Fluid Mech.* **212**, 155 (1990).
- ¹⁷N. A. Hill and M. A. Bees, "Taylor dispersion of gyrotactic swimming micro-organisms in a linear shear flow," *Phys. Fluids* **14**, 2598 (2002).
- ¹⁸A. Manela and I. Frankel, "Generalized Taylor dispersion in suspensions of gyrotactic swimming micro-organisms," *J. Fluid Mech.* **490**, 99 (2003).
- ¹⁹S. Childress, M. Levandowsky, and E. A. Spiegel, "Pattern formation in a suspension of swimming micro-organisms," *J. Fluid Mech.* **69**, 595 (1975).
- ²⁰N. A. Hill, T. J. Pedley, and J. O. Kessler, "Growth of bioconvection patterns in a suspension of gyrotactic micro-organisms in a layer of finite depth," *J. Fluid Mech.* **208**, 509 (1989).
- ²¹E. J. Hinch and L. G. Leal, "The effect of Brownian motion on the rheological properties of a suspension of non-spherical particles," *J. Fluid Mech.* **52**, 683 (1972).
- ²²T. J. Pedley and J. O. Kessler, "The orientation of spheroidal microorganisms swimming in a flow field," *Proc. R. Soc. London, Ser. B* **231**, 47 (1987).
- ²³J. O. Kessler, "Co-operative and concentrative phenomena of swimming microorganisms," *Contemp. Phys.* **26**, 147 (1985).
- ²⁴J. B. Bell, P. Colella, and H. M. Glaz, "A second-order projection method for the incompressible Navier-Stokes equations," *J. Comput. Phys.* **85**, 257 (1989).
- ²⁵D. L. Brown, R. Cortez, and M. L. Minion, "Accurate projection methods for the incompressible Navier-Stokes equations," *J. Comput. Phys.* **168**, 464 (2001).
- ²⁶W. H. Press, S. A. Teukolsky, W. T. Vetterling, and B. P. Flannery, *Numerical Recipes in FORTRAN: The Art of Scientific Computing*, 2nd ed. (Cambridge University Press, New York, 1992).
- ²⁷U. Ghia, K. N. Ghia, and C. T. Shin, "High-Re solutions for incompressible flow using the Navier-Stokes equations and a multigrid method," *J. Comput. Phys.* **48**, 387 (1982).
- ²⁸R. Schreiber and H. B. Keller, "Driven cavity flows by efficient numerical techniques," *J. Comput. Phys.* **49**, 310 (1983).
- ²⁹T. Fusegi, J. M. Hyun, K. Kuwahara, and B. Farouk, "A numerical study of three-dimensional natural convection in a differentially heated cubical enclosure," *Int. J. Heat Mass Transfer* **34**, 1543 (1991).
- ³⁰J. O. Kessler, "Individual and collective fluid dynamics of swimming cells," *J. Fluid Mech.* **173**, 191 (1986).
- ³¹J. O. Kessler, "Path and pattern—The mutual dynamics of swimming cells and their environment," *Commun. Theor. Biol.* **1**, 85 (1989).